Capillarity-driven flows at the continuum limit

Olivier O. Vincent, Alexandre Szenicer, Abraham D. Stroock

Journal Name

ARTICLE TYPE

Cite this: DOI: 10.1039/xxxxxxxxxx

Capillarity-Driven Flows at the Continuum Limit†

Olivier Vincent,[a*] Alexandre Szenicer,[a] and Abraham D. Stroock[a,b‡]

Received Date
Accepted Date

DOI: 10.1039/xxxxxxxxxx

www.rsc.org/journalname

We experimentally investigate the dynamics of capillary-driven flows at the nanoscale, using an original platform that combines nanoscale pores ($\simeq 3$ nm in diameter) and microfluidic features. In particular, we show that drying involves a fine coupling between thermodynamics and fluid mechanics that can be used to generate precisely controlled nanoflows driven by extreme stresses – up to 100 MPa of tension. We exploit these tunable flows to provide quantitative tests of continuum theories (e.g. Kelvin-Laplace equation and Poiseuille flow) across an unprecedented range and we isolate the breakdown of continuum as a negative slip length of molecular dimension. Our results show a coherent picture across multiple experiments including drying-induced permeation flows, imbibition and poroelastic transients.

1 Introduction

Fluids confined at the nanoscale play central roles in many areas of science and technology, from geophysics[1,2], plant hydraulics and biomaterials[3,4] to catalysis and filtration[5,6]. These contexts have motivated considerable effort to understand both the dynamic[7,8] and thermodynamic[9,10] behavior of nano-confined liquids, but fundamental points of debate persist. With respect to dynamics, theoretical considerations suggest that continuum fluid mechanics (Navier-Stokes) should govern flows in conduits greater than ~ 1 nm in lateral dimension[8] but significant uncertainty remains with respect to both constitutive properties and boundary conditions. For example: experiments have only constrained the shear viscosity of water to within a factor of three for confinement below 4 nm[11] and, while simulations indicate that slip lengths should tend to zero on wetting surfaces[12] experimental values typically span -5 to 5 nm[8,13]. With respect to thermodynamics, uncertainty remains regarding the limits of validity of the macroscopic picture of liquid-vapor phase behavior (Kelvin-Laplace) in pores below 10 nm-diameter[14] with increasing importance of solid-fluid interactions and the emergence of inhomogeneities within the liquid[15]. Recently, excellent agreement has been reported between macroscopic predictions and simulations for water desorption in pores < 3 nm in diameter[16] but experimental tests of Kelvin-Laplace with water have only found reasonable agreement for gaps above 10 nm[17,18]. In a situation that couples transport and thermodynamics, capillary-driven flow rates measured by numerous groups deviate significantly (up to 2-fold) from predictions based of macroscopic theory for nanochannels of height below 100 nm[19].

These large uncertainties result in part from the challenges associated with the study of highly confined liquids, such as the difficulty of performing direct measurements of the liquid state at the pore-scale and of generating measurable flows given the small volumes involved and the extreme viscous drag[8]. Surface tension driven flows provide an attractive opportunity due to the large capillary driving forces that can develop spontaneously in nanopores. Imbibition, for example, is a common process where a wetting liquid spontaneously invades a porous medium, and has received recent attention as a tool in nanofluidics[20,21]. Imbibition, however, is unsteady and offers little control over the flow and thermodynamic state of the liquid. Drying is another capillary-related process involved in many natural and technological situations[3,4]. However, despite considerable work on the macroscopic fluid mechanics of drying[22,23] on the one hand, and on the thermodynamics of desorption from nanopores on the other hand[24,25], the dynamics of drying at the nanoscale has only received recent attention[26,27] and remains largely unexplored.

In this article, we investigate drying as an original way to generate controlled flows of highly confined liquids. We propose an experimental platform that couples nanofluidic and microfluidic structures to allow for precise measurements of both drying and imbibition with nanoscale confinement. With this platform, we show quantitatively that the tension (negative pressure) in the liquid predicted by the thermodynamics of unsaturated liquid-vapor equilibria (Kelvin equation) manifests itself as a hydraulic stress out to $\simeq 100$ MPa, a tensile stress that drives large flows despite massive hydraulic resistance. We also show that the result-

[a] Cornell University, Robert Frederick Smith School of Chemical and Biomolecular Engineering, Ithaca, NY, USA
[b] Kavli Institute at Cornell for Nanoscale Science, Ithaca, NY, USA
* E-mail: orv3@cornell.edu
‡ E-mail: ads10@cornell.edu

† Electronic Supplementary Information (ESI) available: the ESI includes details of the platform fabrication, of the experimental procedure, of the analysis methods, and a discussion of alternative hypotheses. Details of the mathematical models presented in the manuscript are also provided. See DOI: 10.1039/b000000x/

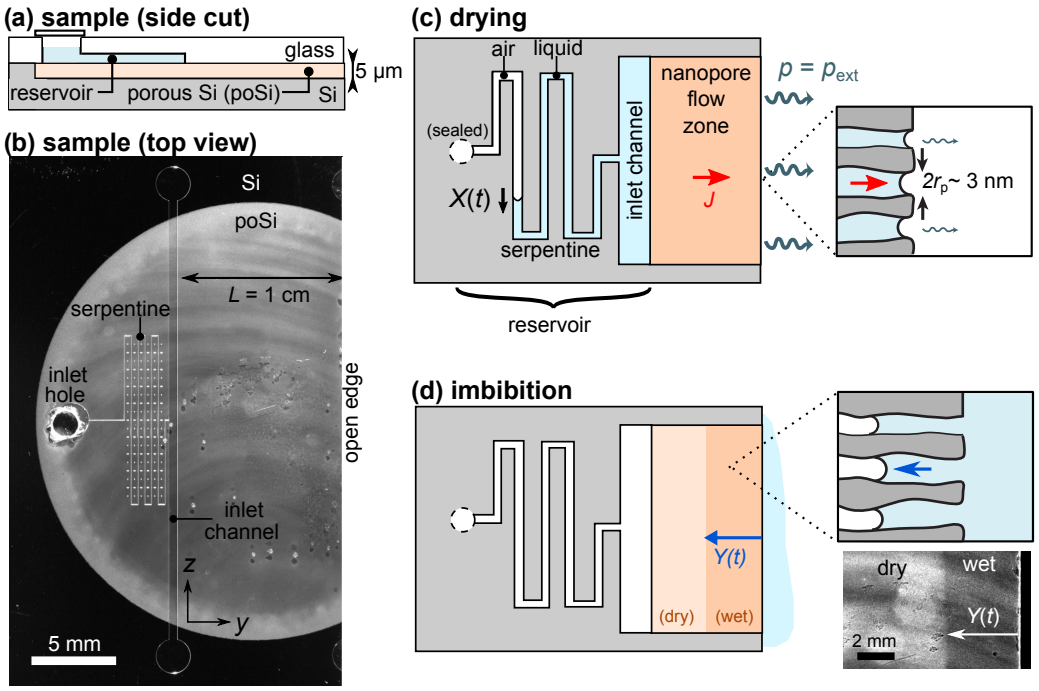

Fig. 1 (a) Side-view sketch and (b) top view photograph of the micro/nano-fluidic platform (see text for details). (c) Drying-induced flows through the nanopores (red arrows, Darcy velocity J) for various externally imposed humidity conditions (controlled vapor pressure at a value $p_{\rm ext}$, corresponding to a relative humidity $p_{\rm ext}/p_{\rm sat}$) were determined from the emptying rate of reservoir by tracking the position $X(t)$ of the air-liquid interface in the serpentine part of the reservoir. (d) Using the same sample after evacuation also allowed for a separate measurement of spontaneous imbibition flows (blue arrows), using the position of the optically-visible wetting front, $Y(t)$. Contrast was enhanced on the micrograph for clarity.

ing permeation follows the continuum laws of capillary-viscous flows provided that a simple correction is included to account for molecular adsorption at the pore wall. Our results thus provide an unusually robust experimental test of transport and thermodynamic models at the continuum limit.

2 Methods

Figure 1a-b presents our sample. Details of the fabrication and of the experimental procedure can be found in the Supporting Information (ESI). Briefly, we used anodization to etch a circular zone in a silicon wafer, leading to a $5.5\,\mu$m-thick layer of isotropic, interconnected pores with a distribution of pore sizes in the range, $r_{\rm p} = 1.4 \pm 0.4$ nm and porosity $\phi = 0.45$ based on N_2 porosimetry. We used lithography in a glass wafer to form a reservoir accessed by an inlet hole drilled through the glass. The reservoir itself included a serpentine-shaped microchannel connected to a long inlet channel. The latter fed liquid to the porous layer that spanned the distance between the inlet channel and the open edge. Finally we bonded silicon to glass and opened the pores to the outside at the edge of the sample by dicing (Fig 1a-b).

We performed drying experiments (Fig 1c) by filling the pores and reservoir with liquid, and then placing the sample in a vapor of controlled humidity (constant partial vapor pressure $p_{\rm ext}$) after sealing the inlet hole. We could evaluate the flow rate through the porous layer due to evaporation from the open edge (right of Fig 1a-b) by measuring the rate of emptying of the reservoir. To do so, we tracked the position of the air-liquid interface in the serpentine-shaped part of the reservoir ($X(t)$ in Fig 1c). The presence of bulk liquid water in the reservoir ensured that the porous area to the left of the inlet channel stayed saturated at all times. As a result, flow in the porous layer occurred only in the zone situated between the inlet channel and the open edge (shaded in orange in Fig 1c), and the tracking of $X(t)$ provided an accurate measurement of the flow rate through the nanopores.

We also performed independent imbibition experiments on the same sample, by submersion in liquid after evacuation (Fig 1d). We monitored the advancing wetting front ($Y(t)$ in Fig 1d) by time-lapse photography, taking advantage of the change of color of the porous silicon layer as a function of its filling state (see micrograph in Fig 1d).

In order to describe the thermodynamic states of liquid and vapor in a unified way, we use *liquid potential*[3], $\Psi = (\mu - \mu_0)/v_{\rm m}$ where μ[J/mol] is the chemical potential, μ_0 is its standard value (corresponding to bulk liquid-vapor equilibrium in air at atmospheric pressure P_0) and $v_{\rm m}(P,T)$ [m^3/mol] is the liquid molar volume. This quantity expresses the chemical potential of each phase as the corresponding pressure of the pure, bulk liquid. Neglecting the pressure dependence of $v_{\rm m}$, an approximation that we expect to hold to within 2.6% for water (see ESI),

$$\begin{cases} \Psi_{\rm liq} = P - P_0 & \text{for the liquid} \\ \Psi_{\rm vap} = \frac{RT}{v_{\rm m}} \ln\left(\frac{p}{p_{\rm sat}}\right) & \text{for the vapor} \end{cases} \quad (1)$$

where P and p represent respectively the liquid and the partial vapor pressures, $p_{\rm sat}(T,P_0)$ is the saturated vapor pressure and RT is the thermal energy.

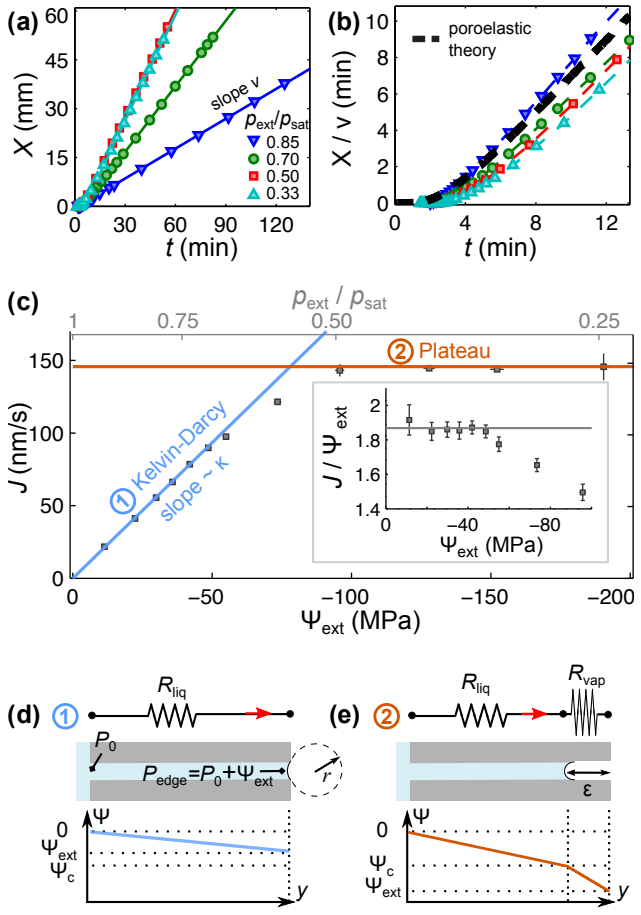

Fig. 2 Drying dynamics with water. (a) Position of the air-water interface in the serpentine-shaped reservoir, $X(t)$, reflecting the loss of water by evaporation at the open edge (Figure 1c). (b) Early transients: data in (a) normalized by the steady-state speed v. The dashed, black curve shows the prediction from the theory of poroelasticity (see ESI). (c) Volumetric flux as a function of the external vapor potential, Ψ_{ext} (bottom axis) calculated with Equation (2) from the imposed relative humidity p_{ext}/p_{sat} (top axis). The lines represent the two predicted regimes from Eqs. (4) and (7). (d-e) Schematic diagrams of our model for these two regimes, with sketches of the spatial profiles of the liquid potential.

3 Results and Discussion

We first recorded drying dynamics at a variety of imposed relative humidities p_{ext}/p_{sat}. The measured emptying dynamics of the reservoir is shown as $X(t)$ in Fig 2a. The results show the establishment of a steady-state after a transient of a few minutes (Fig 2b). From the speed, we used the geometry of the porous layer to calculate the steady-state volumetric flux in the porous medium (Darcy velocity), $J\,[\mathrm{m/s}]$. Data as in Figure 2c revealed two regimes.

We begin by considering the linear regime (① in Figure 2c) with the physical picture of the pore-scale depicted in Figure 2d. Here, we assume that the nano-menisci remained pinned at the open edge of the porous layer and that local equilibrium was established between the pore liquid behind the nano-menisci and the bulk vapor (partial pressure p_{ext}); we expect this equilibrium to hold to good approximation due to the large transport resistance in the porous medium relative to that in the vapor (see ESI). To evaluate this equilibrium, we suppose that, despite the strong confinement imposed by the pores, the properties of the liquid are unperturbed relative to that of a bulk phase. In other words, the pore liquid responds to the lowering of the vapor pressure with a reduction of its hydrostatic pressure, as predicted by the well-known Kelvin equation ($\Psi_{liq}=\Psi_{vap}$ from Equation 1).

$$P_{edge}-P_0=\Psi_{ext}=\frac{RT}{v_m}\ln\left(\frac{p_{ext}}{p_{sat}}\right). \qquad (2)$$

Equation (2) provides an expression for the pressure difference that drives flow through the nanoporous layer between the microchannel ($P=P_0>0$) and the open edge ($P=P_{edge}<0$). This liquid stress has its dynamic origin in capillarity, due to the curvature r^{-1} of the liquid-air interface; compatibility with the phase equilibrium (Equation 2) is ensured through the Kelvin-Laplace relation

$$\Psi_{ext}=-2\sigma r^{-1}. \qquad (3)$$

Here, we neglect both the pressure drop along the microchannel and the capillary pressure associated with the macroscopic air-liquid interface at the channel's left end, such that the pressure of liquid entering the porous layer is approximately atmospheric (see ESI). Assuming Darcy flow[28] through the porous medium, we thus predict linear response of the permeation rate with respect to Ψ_{ext}:

$$J=-\kappa(P_{edge}-P_0)/L=-\kappa\Psi_{ext}/L. \qquad (4)$$

where κ is the Darcy permeability of the porous layer and L is the geometrical length of the permeation path (Figure 1). The blue line and inset in Figure 2c clearly illustrate the robustness of this linear regime down to $\Psi_{ext}\simeq -50$ MPa. We extract the permeability from the best-fit slope: $\kappa=(1.87\pm0.08)\times10^{-17}\,\mathrm{m^2/(Pa.s)}$, a value that is in the lower range of permeability of rocks considered impervious such as granite[28]. We compare this result to Carman-Kozeny theory

$$\kappa=\frac{\phi\, r_{eff}^2}{8\,\eta\,\tau} \qquad (5)$$

where η is the viscosity of the liquid and r_{eff} is an effective pore size[29]. The tortuosity τ is expected to take physically reasonable values close to, $\tau=3$ which would correspond to an ideal isotropic architecture of cylindrical pores[29]. Using the value of κ experimentally determined above and $\tau=3$, we find a preliminary estimate of $r_{eff}\simeq 1.0$ nm, which lies in the lower range of the pore sizes estimated from N_2 porosimetry.

Independently of the pore geometry, we also use the transient responses (Figure 2b) to perform a second check of the value of permeability extracted from the steady-state drying experiments. Poroelastic theory predicts that pressure diffuses through a porous medium with a diffusivity $C=\kappa/(\phi\chi)$ where χ is the effective compressibility of the fluid-filled solid. To generate the black curve in Figure 2b, we used κ estimated above and took for χ the bulk compressibility of liquid water ($4.5\times10^{-10}\,\mathrm{Pa^{-1}}$) (see ESI); the agreement with experiments indicates that we have measured a coherent value of the permeability and that confinement has not strongly perturbed the thermodynamic properties of

the pore liquid.

We now consider the plateau regime of the flow at larger driving forces (② in Figure 2c) with the physical picture depicted in Figure 2e. Once the pressure difference required for equilibrium (Kelvin Equation, Eq. 2) exceeds the capillary pressure that can be maintained by the pores through the variable curvature of the liquid-air nano-menisci at the open edge of the porous layer, we suppose that the nano-menisci recede from the edge and that the flow within the porous medium becomes multiphase – liquid between $y = 0$ and $L - \varepsilon$ (with corresponding linear mass conductance g_{liq} [s] and hydraulic resistance $R_{\mathrm{liq}} = (L-\varepsilon)/g_{\mathrm{liq}}$ [m/s], see ESI), and vapor between $y = L - \varepsilon$ and the open edge at $y = L$ (linear conductance g_{vap}, resistance $R_{\mathrm{vap}} = \varepsilon/g_{\mathrm{vap}}$). Using the Laplace equation for the capillary pressure (Eq. 3) and considering that the maximum meniscus curvature allowed in a pore of radius r_{p} with equilibrium contact angle θ is $r^{-1} = \cos\theta/r_{\mathrm{p}}$, this retreat of the nano-menisci occurs when $\Psi_{\mathrm{ext}} < \Psi_{\mathrm{c}}$ where

$$\Psi_{\mathrm{c}} = -2\sigma\cos\theta/r_{\mathrm{p}}. \tag{6}$$

The receding of the nano-menisci stops at a distance ε from the edge at which phase equilibrium can be satisfied again, i.e. at a location where the liquid potential is equal to Ψ_{c}, given the imposed boundary conditions $\Psi(0) = 0$ at the reservoir level and $\Psi(L) = \Psi_{\mathrm{ext}}$ at the open edge. This new steady-state position $\varepsilon(\Psi_{\mathrm{ext}})$ is thus found by satisfying $\Psi(L-\varepsilon) = \Psi_{\mathrm{c}}$ given the resistors-in-series configuration of Figure 2e. Based on Darcy's law for the liquid phase and Knudsen diffusion for the vapor phase, we estimate $g_{\mathrm{vap}}/g_{\mathrm{liq}} \simeq 10^{-4}$ which implies $\varepsilon/L \sim g_{\mathrm{vap}}/g_{\mathrm{liq}} \ll 1$ (see ESI). It follows that the vapor-liquid interface stays close to the edge, resulting in a pressure gradient in the liquid phase equal to $\Psi_{\mathrm{c}}/(L-\varepsilon) \simeq \Psi_{\mathrm{c}}/L$, leading to

$$J_{\mathrm{c}} = -\kappa\Psi_{\mathrm{c}}/L \tag{7}$$

to excellent approximation. The flow predicted by Equation (7) is independent of the imposed external condition (vapor pressure p_{ext}); this independence explains the plateauing of the drying flux observed experimentally at low values of relative humidity, $p_{\mathrm{ext}}/p_{\mathrm{sat}}$ (Figure 2c). In this regime the driving force for the flow is set by the intrinsic capillary pressure of the pores Ψ_{c} instead of Kelvin pressure Ψ_{ext}.

Comparing Eqs. (4) and (7), we remark that Ψ_{c} corresponds to the intersection point between the two regimes ① and ② and thus provides an independent measure of the capillary pressure $\Psi_{\mathrm{c}} = -76 \pm 5$ MPa. Using Laplace law (Equation 6) with $\theta = 25 \pm 5^{\circ}$ (see ESI) then yields a new pore size estimate $r_{\mathrm{p,c}} = 1.7 \pm 0.2$ nm. This value agrees well with the range estimated from N_2 porosimetry, but there is an apparent inconsistency with the pore radius $r_{\mathrm{eff}} = 1.0$ nm deduced from Carman-Kozeny equation (5).

In order to resolve this conflict and check the validity of our interpretation of the drying regimes, we measured imbibition dynamics in the same sample (Figure 1d). During imbibition of a dry sample, the liquid front position is expected to follow $Y(t) = \sqrt{wt}$ with

$$w = -\frac{2\kappa\Psi_{\mathrm{c}}}{\phi} \tag{8}$$

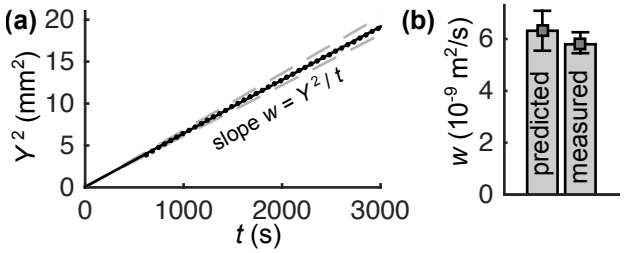

Fig. 3 Imbibition with water. (a) Front position $Y^2(t)$. The grey dashed lines represent the uncertainty from the image analysis (see ESI). (b) Comparison between the measured imbibition speed w and the prediction from Equation (8), using the values of κ and Ψ_{c} deduced from the drying experiments.

known as the Lucas-Washburn (LW) law[30]. Interestingly, the two important parameters governing imbibition dynamics are precisely the permeability κ and the intrinsic capillary pressure Ψ_{c} estimated from the drying analysis above. Figure 3a shows that imbibition in our system followed the LW $\sqrt{t}$ scaling and quantitatively agreed with Equation (8), using the values of κ and Ψ_{c} estimated from drying (Figure 3b). This result confirms the appropriateness of our interpretation and analysis of the drying regimes. This analysis allows the independent extraction of both viscous (κ) and capillary (Ψ_{c}) contributions, a feature not accessible with imbibition experiments that only access the product $\kappa \times \Psi_{\mathrm{c}}$ (see Equation 8).

To resolve the apparent contradiction in the pore size estimates, we could adjust the tortuosity to a larger value ($\tau \sim 10$) to reconcile Equation (5) with $r_{\mathrm{eff}} = 1.7$ nm, but such a value of τ seems unphysically high[29] (see ESI). Alternatively, we note that Equation (5) is based on the assumption of a developed Poiseuille flow in the pores with a zero-velocity (no-slip) condition at the pore wall. However, large deviations to the no-slip boundary conditions have been reported at the nanoscale[7,8] and described with the concept of slip length δ which accounts for slippage ($\delta > 0$) or sticking ($\delta < 0$) of the fluid at the wall. The hydrodynamic radius across which the Poiseuille flow profile is established is then $r_{\mathrm{h}} = r_{\mathrm{p}} + \delta$ and the effective radius in Carman-Kozeny equation (5) becomes[29]

$$r_{\mathrm{eff}} = \frac{r_{\mathrm{h}}^2}{r_{\mathrm{p}}} = r_{\mathrm{p}}\left(1 + \frac{\delta}{r_{\mathrm{p}}}\right)^2. \tag{9}$$

The value $r_{\mathrm{eff}} = 1.0$ nm estimated previously is compatible with a pore size of $r_{\mathrm{p}} = 1.7$ nm if a negative slip length of $\delta = r_{\mathrm{p}} - r_{\mathrm{h}} = -0.4$ nm is used. Interestingly, this value is close to the typical thickness of a monolayer of water molecules, as can be estimated from $d_{\mathrm{w}} = (v_{\mathrm{m}}/\mathcal{N}_{\mathrm{a}})^{1/3} = 0.31$ nm, where $\mathcal{N}_{\mathrm{a}}$ is Avogadro's number. This correspondence suggests that a monolayer of water molecules could be immobilized at the pore wall (Figure 4a), as has been proposed for nanoporous glasses[29,31].

To investigate these hypotheses further and isolate the contributions of boundary conditions from those of the geometrical tortuosity, we measured both J_{c} (plateau-drying) and w (imbibition) for 3 additional liquids (acetone, ethanol, and isopropanol) of larger size ($d = 0.46 - 0.50$ nm) and a variety of surface tensions and viscosities (Table S1 in ESI). From Eqs. (5–9), both rates

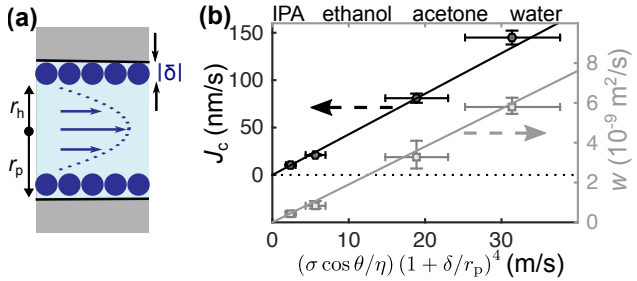

Fig. 4 (a) The hydraulic radius r_h across which the parabolic flow is established differs from the geometrical pore radius r_p by a slip length, δ (negative for an immobile layer). (b) Plateau-drying (black circles) – as in Figure 2c, regime ② – and imbibition (grey squares) – as in Figure 3 – dynamics as a function of the rescaled visco-capillary driving force. Continuous black and grey lines are predictions from Eqs. (7) and (8) respectively, using Equation (5) with a unique value of tortuosity, $\tau = 4.5$.

should vary in proportion to the following grouping of liquid-dependent properties: $(\sigma\cos\theta/\eta) \times (1+\delta/r_p)^4$ with $\delta = -d$. The plot in Figure 4b shows that the rates collapse onto straight lines across the series of four liquids when the macroscopic values of σ, θ, and η and $\delta = -(v_m/\mathcal{N}_a)^{1/3}$ are used, and with $r_p = r_{p,c} = 1.7 \pm 0.2$ nm. This collapse, independent of the choice of tortuosity, confirms that sticking of a mono-molecular layer can explain the observed dynamics. Further, the best-fit slope of each line provides a consistent value of $\tau = 4.5$ (via Eqs. S20 and S21 in ESI) for both imbibition and drying, a value that is physically reasonable for non-ideal pore architectures.

We note that other scenarios involving fine tuning of the liquid parameters (e.g. η, σ, see section V in ESI) could be invoked to accommodate our observations. However, we favor the hypothesis of an immobile monolayer of liquid, which allows us to reproduce all of our experiments across methods and liquids with the bulk liquids' properties and no adjustable parameters. We also remark that our model can be extended in a completely coherent manner to a distribution of pore sizes (see ESI).

4 Conclusions

In conclusion, we have demonstrated for the first time the use of drying to precisely and independently measure viscous and capillary effects at the nanoscale. We found an unusual coherency which contrasts the large deviations from theory reported for nanoscale flows even in much larger conduits[8,19]. We also demonstrated that the thermodynamic stress implied by Kelvin equation expresses itself as a mechanical pressure in the liquid even in pores that measure just $6-10$ molecules in diameter. While this mechanical equivalence of the Kelvin stress has been shown to hold in static situations[17,32,33], our results provide the first demonstration in a dynamic context (permeation flows) and across an unprecedented range of stresses (down to $\simeq -100$ MPa).

In technological contexts, the two regimes of passive evaporation-driven flow elucidated here have direct implications for the precise control of fluid flow in micro and nanosystems[8] and membrane science[4]. Our results also show that nanoporous solids can be a promising alternative to hydrogels for the development of biomimetic systems that use liquids under large negative pressures similarly to plants[34]. Finally, in geophysical contexts, our experimental platform provides a new basis for evaluating the role of capillary phenomena in controlling the mobility of fluids within reservoirs exploited in, for example, hydraulic fracturing[2] and sequestration of carbon dioxide[1].

Acknowledgements

The authors thank Eugene Choi for the measurement of nitrogen isotherms and Glenn Swan for technical assistance. This work was supported by the National Science Foundation (IIP-1500261), the Air Force Office of Scientific Research (FA9550-15-1-0052), the U.S. Department of Agriculture (2015-67021-22844) and the Camille Dreyfus Teacher-Scholar Awards program, and was performed in part at the Cornell NanoScale Facility, a member of the National Nanotechnology Infrastructure Network (National Science Foundation; Grand No. ECCS-15420819).

References

1 E. Saadatpoor, S. Bryant and K. Sepehrnoori, *Transport in Porous Media*, 2010, **82**, 3–17.
2 D. T. Birdsell, H. Rajaram, D. Dempsey and H. S. Viswanathan, *Water Resources Research*, 2015, **51**, 1–30.
3 A. D. Stroock, V. V. Pagay, M. A. Zwieniecki and N. M. Holbrook, *Annu. Rev. Fluid Mech.*, 2014, **46**, 615–642.
4 F. Fornasiero, D. Tang, A. Boushehri, J. Prausnitz and C. Radke, *Journal of Membrane Science*, 2008, **320**, 423–430.
5 Y. Li and G. A. Somorjai, *Nano Lett.*, 2010, **10**, 2289–2295.
6 I. Mohmood, C. Lopes, I. Lopes, I. Ahmad, A. Duarte and E. Pereira, *Environmental Science and Pollution Research*, 2013, **20**, 1239–1260.
7 P. Huber, *Journal of Physics: Condensed Matter*, 2015, **27**, 103102.
8 L. Bocquet and E. Charlaix, *Chem. Soc. Rev.*, 2010, **39**, 1073–1095.
9 L. D. Gelb, K. E. Gubbins, R. Radhakrishnan and M. Sliwinska-Bartkowiak, *Reports on Progress in Physics*, 1999, **62**, 1573.
10 G. H. Findenegg, S. Jähnert, D. Akcakayiran and A. Schreiber, *ChemPhysChem*, 2008, **9**, 2651–2659.
11 U. Raviv, P. Laurat and J. Klein, *Nature*, 2001, **413**, 51–54.
12 D. M. Huang, C. Sendner, D. Horinek, R. R. Netz and L. Bocquet, *Phys. Rev. Lett.*, 2008, **101**, 226101.
13 C. D. F. Honig and W. A. Ducker, *Phys. Rev. Lett.*, 2007, **98**, 028305.
14 A. V. Neimark, P. I. Ravikovitch and A. Vishnyakov, *Journal of Physics: Condensed Matter*, 2003, **15**, 347.
15 Y. Long, M. Śliwińska Bartkowiak, H. Drozdowski, M. Kempiński, K. A. Phillips, J. C. Palmer and K. E. Gubbins, *Colloids and Surfaces A: Physicochemical and Engineering Aspects*, 2013, **437**, 33 – 41.
16 M. H. Factorovich, E. G. Solveyra, V. Molinero and D. A. Scherlis, *The Journal of Physical Chemistry C*, 2014, **118**, 16290–16300.
17 L. Fisher and J. Israelachvili, *Chemical Physics Letters*, 1980, **76**, 325–328.

18 M. M. Kohonen and H. K. Christenson, *Langmuir*, 2000, **16**, 7285–7288.
19 F. Chauvet, S. Geoffroy, A. Hamoumi, M. Prat and P. Joseph, *Soft Matter*, 2012, **8**, 10738–10749.
20 S. Gruener and P. Huber, *Phys. Rev. Lett.*, 2009, **103**, 174501.
21 L. N. Acquaroli, R. Urteaga, C. L. A. Berli and R. R. Koropecki, *Langmuir*, 2011, **27**, 2067–2072.
22 F. Chauvet, P. Duru, S. Geoffroy and M. Prat, *Phys. Rev. Lett.*, 2009, **103**, 124502.
23 P. Lehmann, S. Assouline and D. Or, *Phys. Rev. E*, 2008, **77**, 056309.
24 P. I. Ravikovitch and A. V. Neimark, *Langmuir*, 2002, **18**, 9830–9837.
25 D. Wallacher, N. Künzner, D. Kovalev, N. Knorr and K. Knorr, *Phys. Rev. Lett.*, 2004, **92**, 195704.
26 C. Duan, R. Karnik, M.-C. Lu and A. Majumdar, *Proceedings of the National Academy of Sciences*, 2012, **109**, 3688–3693.
27 O. Vincent, D. A. Sessoms, E. J. Huber, J. Guioth and A. D. Stroock, *Phys. Rev. Lett.*, 2014, **113**, 134501.
28 J. Bear, *Dynamics of Fluids in Porous Media*, Courier Dover Publications, 1988.
29 S. Gruener, T. Hofmann, D. Wallacher, A. V. Kityk and P. Huber, *Phys. Rev. E*, 2009, **79**, 067301.
30 *Wicking in Porous Materials: Traditional and Modern Modeling Approaches*, ed. R. Masoodi and K. M. Pillai, CRC Press, 2013.
31 S. Xu, G. C. Simmons, T. S. Mahadevan, G. W. Scherer, S. H. Garofalini and C. Pacheco, *Langmuir*, 2009, **25**, 5084–5090.
32 C. H. Amberg and R. McIntosh, *Canadian Journal of Chemistry*, 1952, **30**, 1012–1032.
33 G. Y. Gor, L. Bertinetti, N. Bernstein, T. Hofmann, P. Fratzl and P. Huber, *Applied Physics Letters*, 2015, **106**, 261901.
34 T. D. Wheeler and A. D. Stroock, *Nature*, 2008, **455**, 208–212.